Supplementary Information for

Dynamic Heterostructure Designing of MnO₂ for High-Performance Aqueous Zinc-Ion Batteries

Xiaoru Zhao [a], Feng Zhang [a], Houzhen Li [a], Huitong Dong [a], Chuncheng Yan [a], Chao Meng [a], Yuanhua Sang [a], Hong Liu *[ab], Yu-Guo Guo*[cd], Shuhua Wang *[a]

a. State Key Laboratory of Crystal Materials, Shandong University, Jinan 250100, P. R. China.

b. Jinan Institute of Quantum Technology, Jinan Branch, Hefei National Laboratory, Jinan, 250101, China.

c. CAS Key Laboratory of Molecular Nanostructure and Nanotechnology CAS Research/Education Center for Excellence in Molecular Sciences, Institute of Chemistry Chinese Academy of Sciences (CAS), Beijing 100190, P. R. China.

d. School of Chemical Sciences, University of Chinese Academy of Sciences, Beijing 100049, P. R. China.

*E-mail: hongliu@sdu.edu.cn ; ygguo@iccas.ac.cn; wangshuhua2019@sdu.edu.cn

Synthesis of BiO/MnO$_2$. BiO/MnO$_2$ was synthesized by a hydrothermal method. Bi(NO$_3$)$_3$•5H$_2$O, KMnO$_4$, and 0.1 mol/L citric acid solution (CA, 10 ml) with a molar ratio of 4:10:1 were dissolved in deionized water (70 ml) and magnetically stirred for about 60 min to form a homogeneous mixture. Then, the obtained solution was transferred to a 100 mL Teflon-lined stainless autoclave and reacted at 180 °C for 12 hours. The reaction products were naturally cooled to room temperature and then alternately washed by centrifugation with ethanol and deionized water for several times. Finally, the precipitation was freeze-dried to obtain BiO/MnO$_2$ material.

Synthesis of δ-BMO. In a typical experiment, δ-BMO was traditional synthesized by a hydrothermal method. Bi(NO$_3$)$_3$•5H$_2$O, KMnO$_4$, and 0.1 mol/L citric acid solution (CA, 10 ml) with a molar ratio of 1:10:1 were dissolved in deionized water (70 ml) and magnetically stirred for about 60 min to form a homogeneous mixture. Then, the obtained solution was transferred to a 100 mL Teflon-lined stainless autoclave and reacted at 180 °C for 12 hours. The reaction products were naturally cooled to room temperature and then alternately washed by centrifugation with ethanol and deionized water for several times. Finally, the precipitation was freeze-dried to obtain δ-BMO material.

Material characterizations. The microstructure and elemental composition of the samples were characterized by scanning electron microscope (SEM, S-4800) and transmission electron microscope (TEM, JEM-2100F). Crystallographic data of the samples were recorded by X-ray diffraction (XRD) on a Bruker-D2 Advance instrument, with Cu Kα radiation (λ = 1.5418 Å) at a scan rate of 0.02 °/s. The in-situ XRD pattern was determined by in-situ x-ray diffractometer (X'Pert3 Powder & XRK-900). X-ray photoelectron spectroscopy (XPS) was collected on the AXIS SUPRA. The C 1s at 284.8 eV was used as a calibration reference. The lattice water content was evaluated by thermogravimetric analysis (TA Discovery TGA 550) at a temperature ramping rate of 10 °C min^{-1} from room temperature to 800 °C. Raman spectrum was

recorded for sample using Horiba LabRAM HR Evolution with excitation laser wavelength at 633 nm.

Battery composition. The active material, carbon black, and polyvinylidene fluoride (PVDF) are mixed in the N-methyl-2-pyrrolidone (NMP) solvent at a ratio of 7:1.5:1.5. After mixing uniformly, the slurry was coated on a 20 μm thick titanium foil to prepare the cathode, and the active material loading is $1 \sim 2$ mg cm^{-2}. The electrochemical performance of CR2032 coin-type battery was studied by using BiO/MnO_2 or δ-BMO as cathode, zinc foil as the anode, glass fiber as the membrane. The electrolyte was 3M $ZnSO_4$ + 0.5M $MnSO_4$ in a solvent of H_2O.

Electrochemical performance test. The electrochemical performance of the assembled battery was tested on the LAND battery testing system (CT2001A) with a voltage range from 0.8 to 1.9 V. Cyclic voltammograms (CV) and electrochemical impedance spectrum (EIS) were measured using CHI 600E electrochemical workstation. EIS measurements were made at open circuit voltage with an AC amplitude of 10 mV, and the frequency range is 0.01 Hz to 100 kHz. Unless otherwise specified, all of the electrochemical tests were conducted at room temperature.

Density functional theory calculations. First-principle calculation was performed in the framework of density functional theory as implemented in the VASP program [1]. The generalized gradient approximation proposed by Perdew, Burke, and Ernzerhof is selected for the exchange-correlation potential [2]. The energy criterion is set to 10^{-4} eV in iterative solution of the Kohn-Sham equation. For all models the vacuum space along the z-direction was set to be 15 Å, which was enough to avoid interaction between the two neighboring images. The Brillouin zone integration is performed using a 2×2×1 k-mesh and a cutoff energy of 450 eV was employed. All the structures are relaxed until the residual forces on the atoms have declined to less than 0.02 eV/Å. The Van der Waals dispersion-corrected DFT was also carried out, as proposed by Grimme et al [3].

The cut-off energy for plane wave is set to 450 eV. The energy criterion is set to

10^{-4} eV in iterative solution of the Kohn-Sham equation. The cell dimensions (a×b×c) are as follows: 3 × 3 × 1 for Bi (012). For all models the vacuum space along the z-direction was set to be 15 Å, which was enough to avoid interaction between the two neighboring images. The Brillouin zone integration is performed using a 2×2×1 k-mesh. All the structures are relaxed until the residual forces on the atoms have declined to less than 0.02 eV/Å. The Gibbs free energy diagrams were estimated by the following equation:

$$\Delta G_i = \Delta E + \Delta ZPE - T\Delta S$$

where ΔE is the energy difference from reactants to products, obtained from DFT calculations; ΔZPE and ΔS are the contributions to the free energy from the zero-point vibration energy and entropy, respectively. T is 298.15 K.
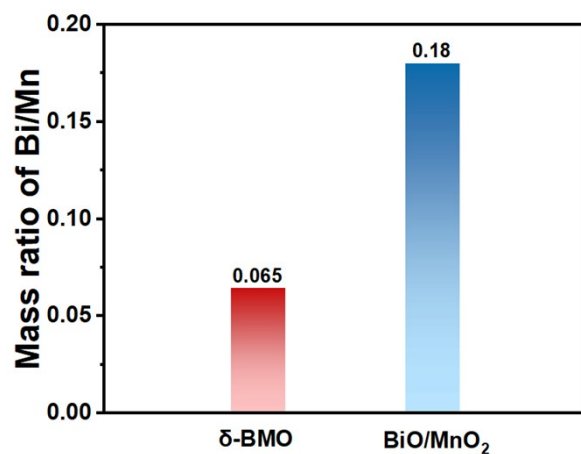
Figure S1. Mass ratios of Bi/Mn in δ-BMO and BiO/MnO$_2$.
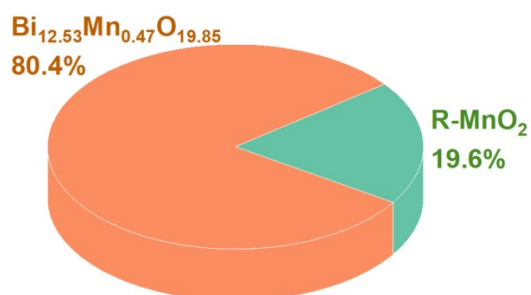
Figure S2. Semi-quantitative analysis of BiO/MnO$_2$.
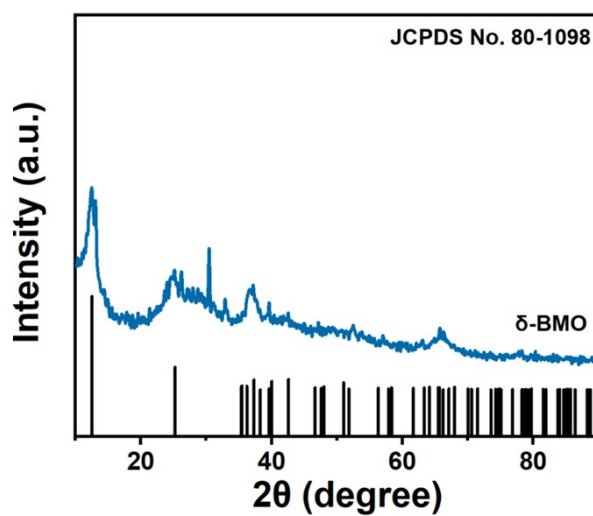
Figure S3. XRD pattern of δ-BMO.
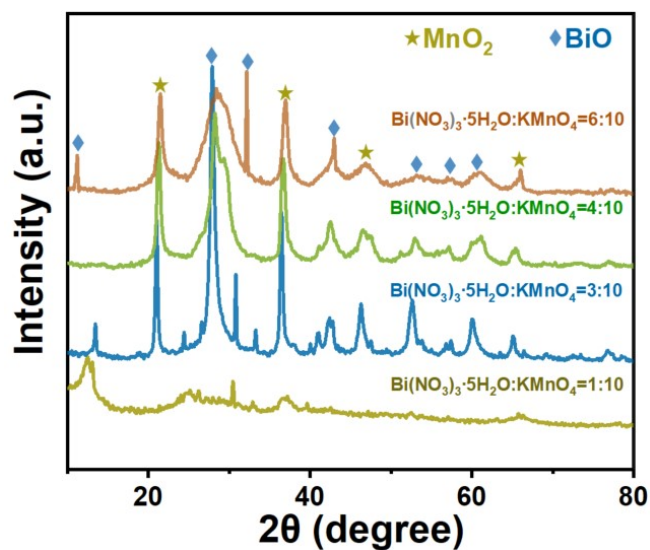
Figure S4. XRD pattern of reactants synthesized with different molar ratios of

$Bi(NO_3)_3 \cdot 5H_2O$ to $KMnO_4$.
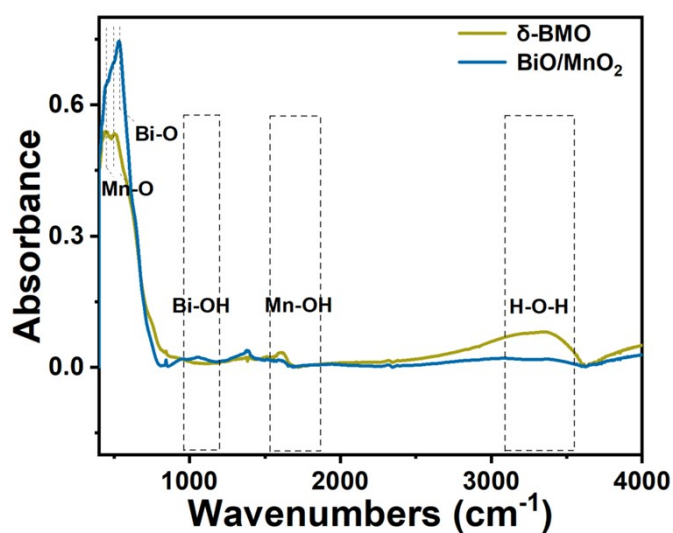
Figure S5. FTIR spectra of δ-BMO and BiO/MnO_2.
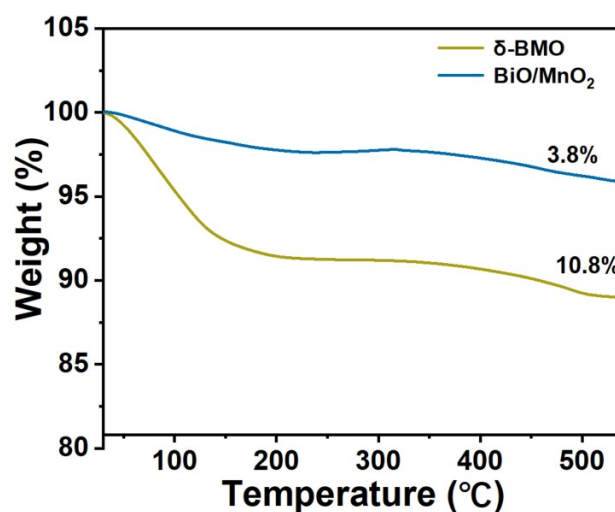
Figure S6. Thermogravimetric analysis curves of δ-BMO and BiO/MnO_2.
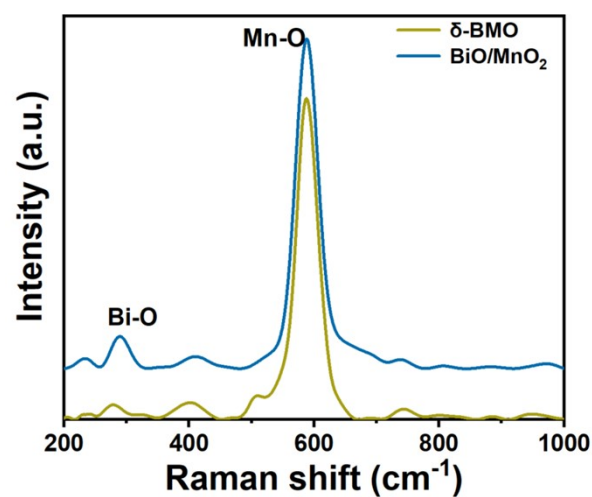
Figure S7. Raman spectra of δ-BMO and BiO/MnO$_2$.
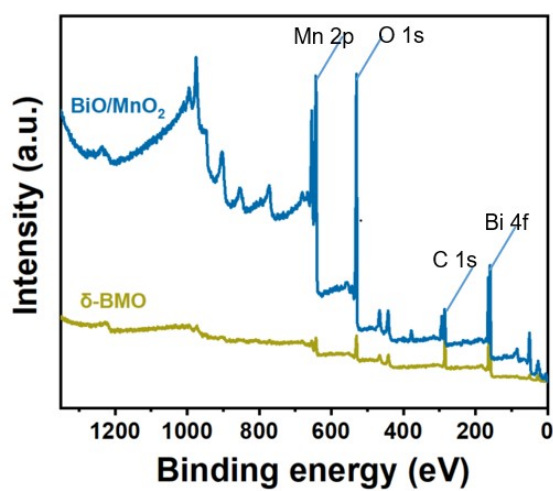
Figure S8. Overall XPS spectrum of δ-BMO and BiO/MnO$_2$.
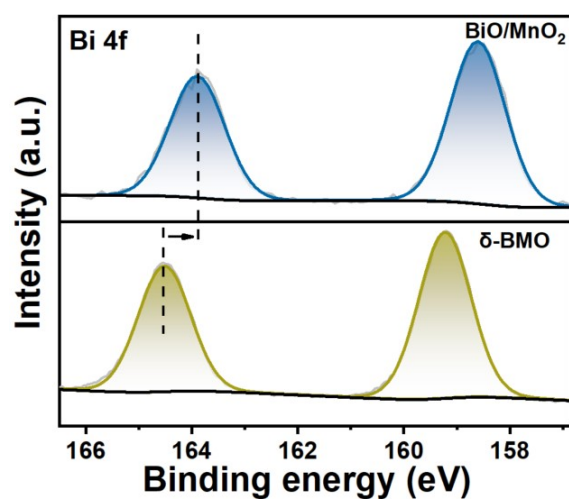
Figure S9. Bi 4f XPS spectra of pristine δ-BMO and BiO/MnO$_2$.
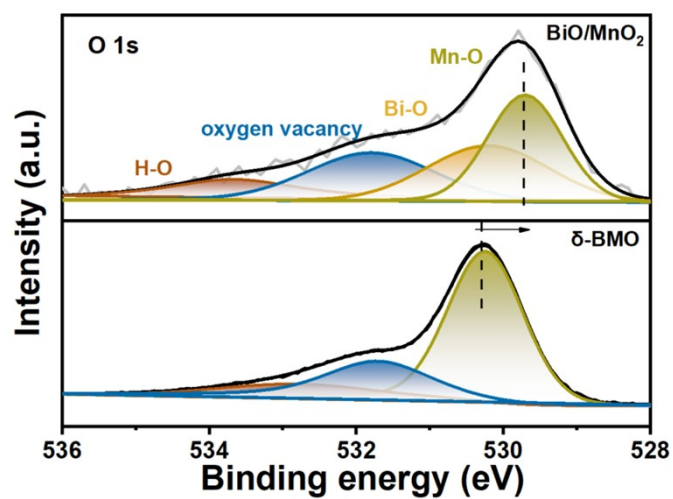
Figure S10. O 1s XPS spectra of pristine δ-BMO and BiO/MnO₂.
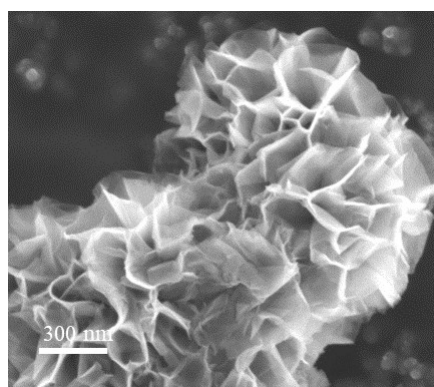
Figure S11. SEM image of δ-BMO.
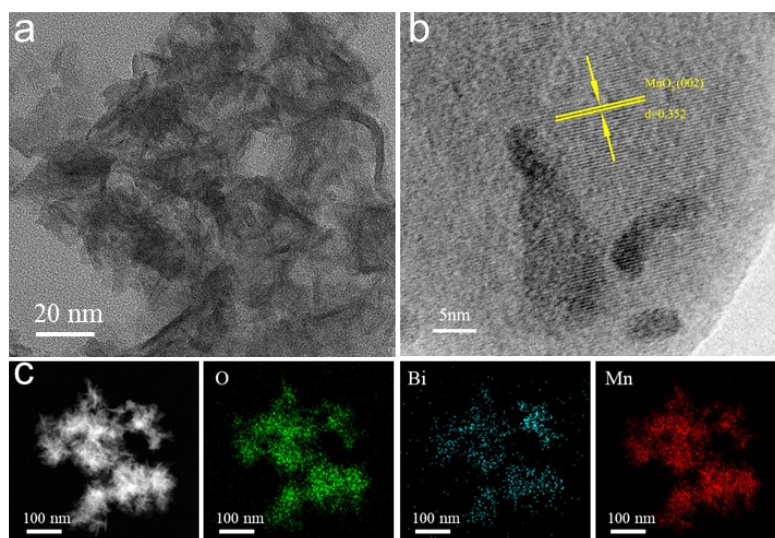
Figure S12. (a) TEM image of δ-BMO. (b) HRTEM image. (c) Corresponding elemental mappings of Mn, O and Bi on δ-BMO.
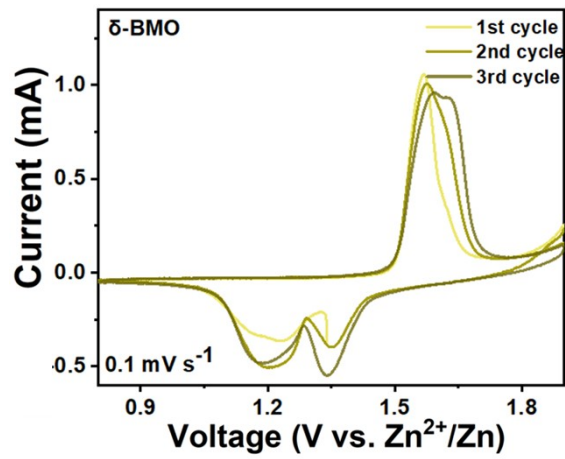
Figure S13. CV curves of δ-BMO at a scan rate of 0.1 mV s^{-1}.
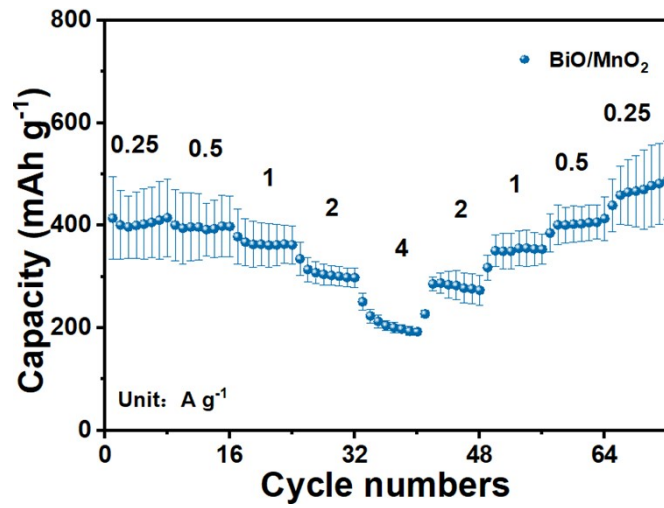
Figure S14. Rate performance with error bars of BiO/MnO$_2$.
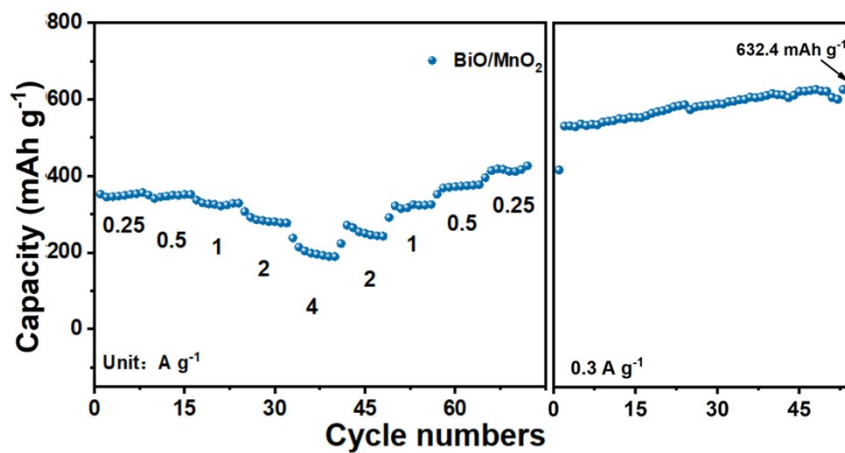
Figure S15. Rate performance after BiO/MnO$_2$ was activated for 5 cycles and cycling performance after rate performance at a current density of 0.3 A g^{-1}.
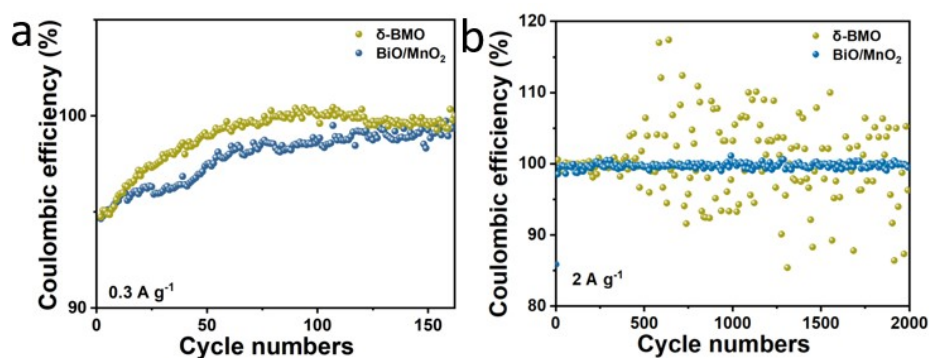
Figure S16. Coulomb efficiency of BiO/MnO$_2$ and δ-BMO (a) at 0.3 A g^{-1}, and (b) at 2 A g^{-1}.
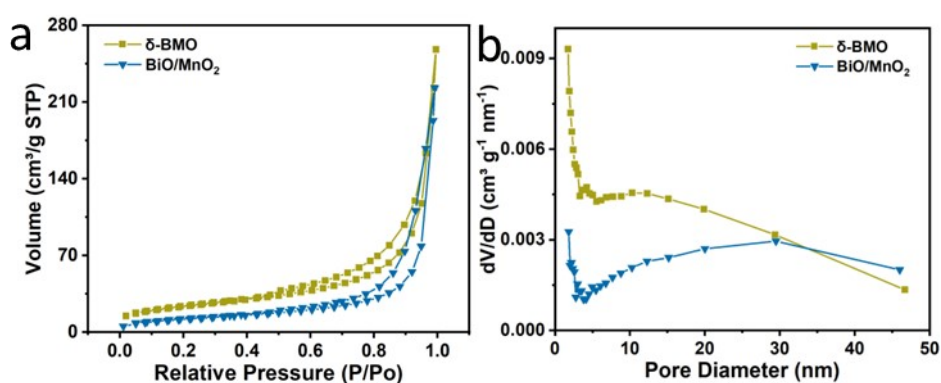
Figure S17. (a) nitrogen adsorption–desorption isotherms of δ-BMO and BiO/MnO$_2$. (b) pore size distributions of δ-BMO and BiO/MnO$_2$.

The BiO/MnO$_2$ material exhibits a smaller surface area of 43.74 m² g^{-1} and larger mesopore structures with an average aperture diameter of 31.55 nm, in comparison to the specific surface area (83.66 m² g^{-1}) and pore diameter (19.08 nm) of δ-BMO. The limited specific surface area impedes the rapid infiltration of electrolyte into the interior of the electrode, thereby explaining the lower initial capacity of BiO/MnO$_2$ (171.3 mA h g^{-1}) compared to δ-BMO (262.5 mA h g^{-1}) at a low current density of 0.3 A g^{-1}(Figure 2f).
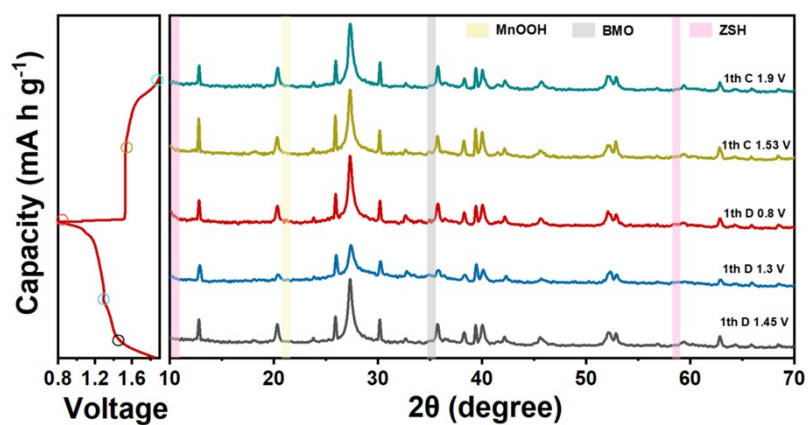
Figure S18. Ex-situ XRD patterns of the intial cycle for BiO/MnO$_2$.
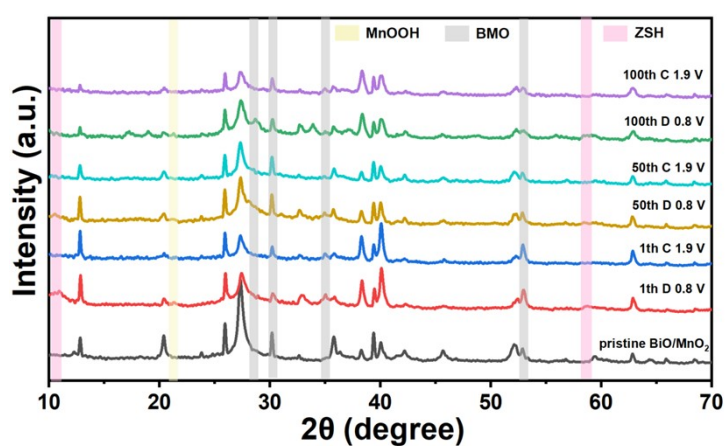
Figure S19. Ex-situ XRD patterns of BiO/MnO$_2$ at different charge and

discharge states from 1 to 100 cycles.
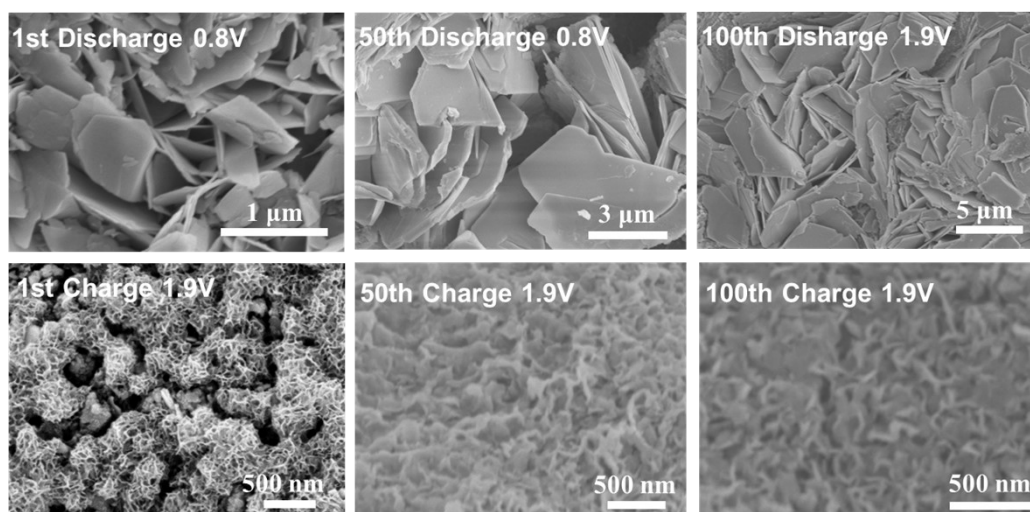
Figure S20. (a-f) SEM images for the morphological evolution at different cycles of
BiO/MnO$_2$.
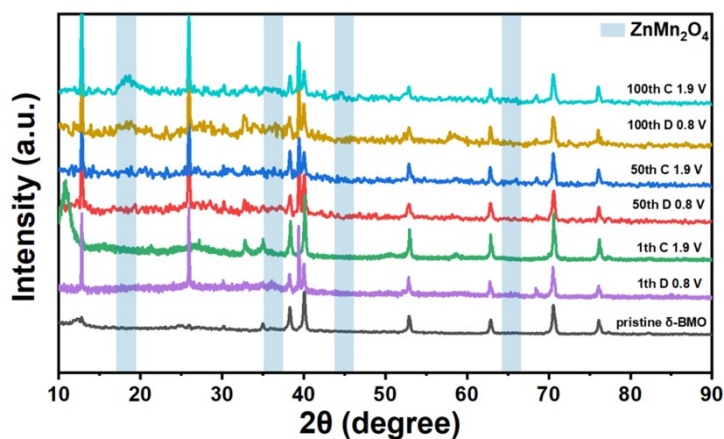
Figure S21. Ex-situ XRD patterns of δ-BMO at different charge and discharge states from 1 to 100 cycles.
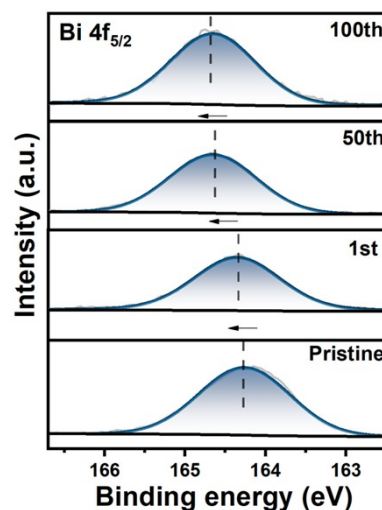
Figure S22. Ex-situ Bi 4f XPS spectra of BiO/MnO$_2$ at different cycles.
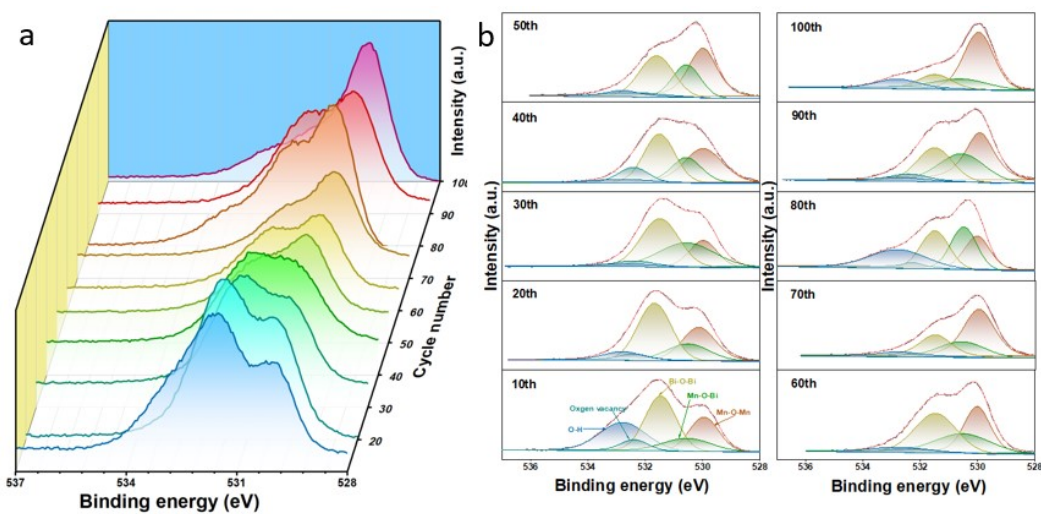
Figure S23. (a) Ex-situ O 1s XPS spectra at different cycles of BiO/MnO$_2$. (b) O 1s XPS spectra of fitting into five peaks.
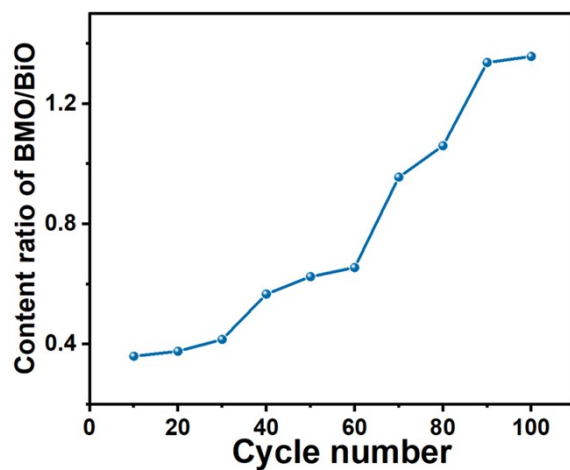
Figure S24. Content ratio of BMO/BiO.
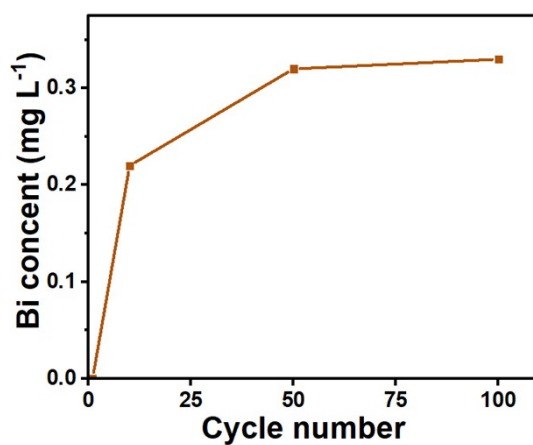
Figure S25. Mass contents of dissolved Bi in 3.0 M $ZnSO_4$ + 0.5 M $MnSO_4$

electrolyte for BiO/MnO_2.
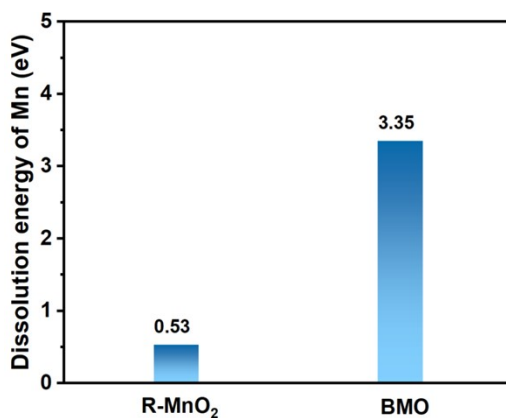
Figure S26. Dissolution energy of Mn in BMO and $R\text{-}MnO_2$.
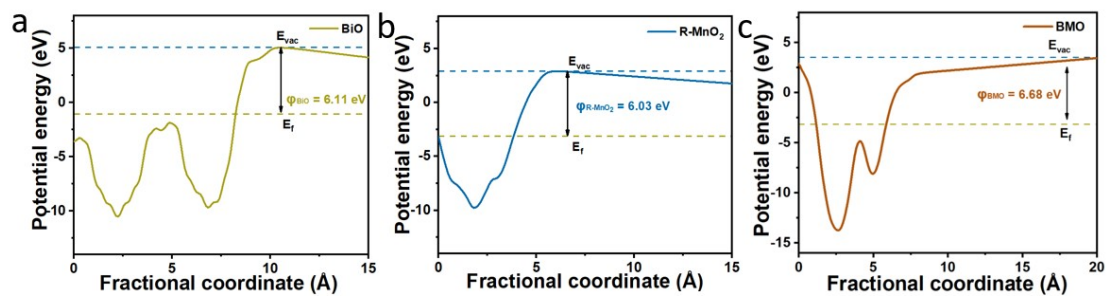
Figure S27. Surface work function and E_F of (a) BiO, (b) R-MnO$_2$, and (c) BMO.
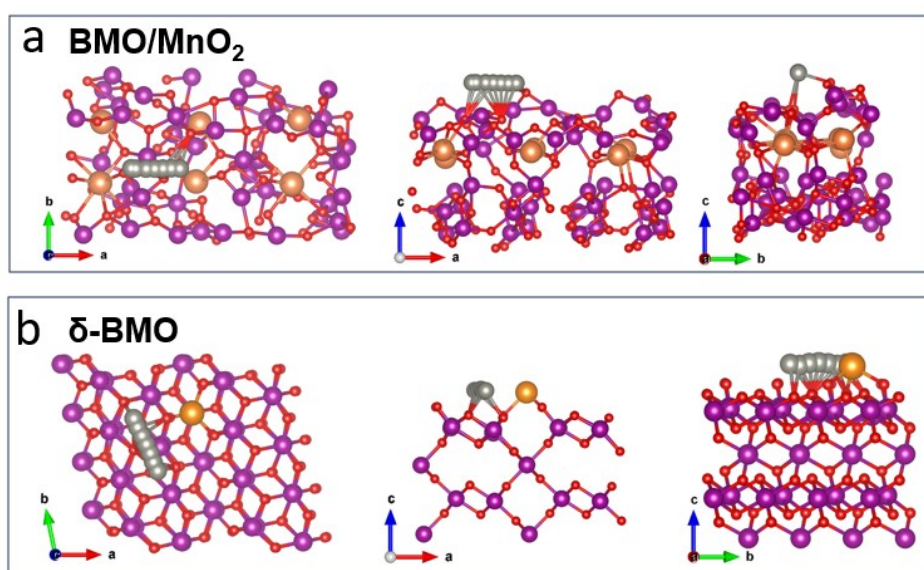
Figure S28. Zn^{2+} diffusion pathway (a) in BMO/MnO$_2$, and (b) in δ-BMO.
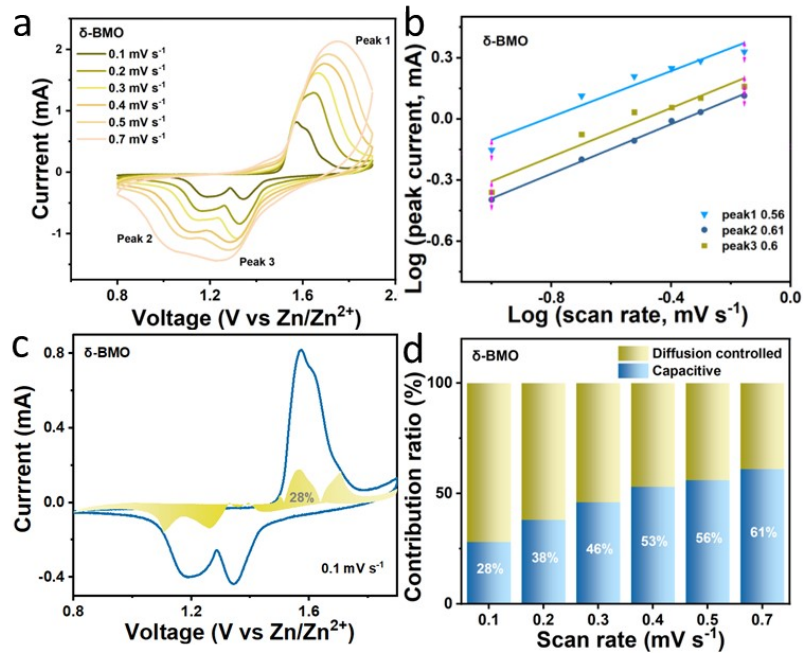
Figure S29. (a) CV curves of the δ-BMO electrode at different scan rates. (b) Log i and log v plots at specific peak currents of the δ-BMO. (c) CV curve with the capacitive-like fraction at a scan rate of 0.1 mV s^{-1} of the δ-BMO. (d) Contribution ratios of capacitive-like and diffusion-controlled capacities at different scan rates.
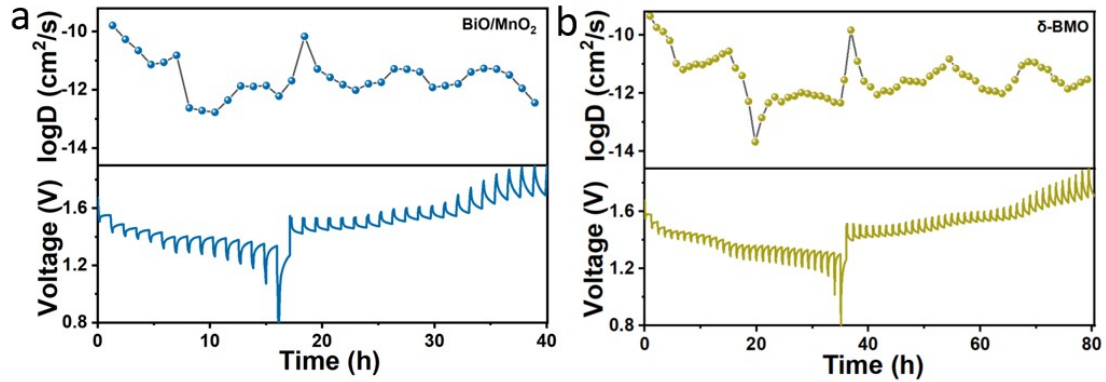
Figure S30. GITT profiles and corresponding ion diffusion coefficients of (a) BiO/MnO$_2$, and (b) δ-BMO cathode.

Table S1. The crystallographic information on the materials.

Sample	Molecular formula	Crystal system	Space group	a (Å)	b (Å)	c (Å)
BiO	Bi$_{12.53}$Mn$_{0.47}$O$_{19.85}$	Cubic	I23(197)	10.153	10.153	10.153
R-MnO$_2$	R-MnO$_2$	Orthorhombic	Pnma (62)	2.864	4.7	9.531

BMO	$Bi_2Mn_4O_{10}$	Orthorhombic	Pbam (55)	7.54	8.534	5.766
δ-BMO	δ-MnO_2	Monoclinic	C2/m (12)	5.149	2.843	7.716

The structure information of these materials was also supplemented sin the revised manuscript. According to the literature, for BiO structure, each cell of BiO contains two molecular formulas: one is a deformed Bi-O polyhedron formed by the coordination of Bi ions and five oxygen ions. The other is the $Bi_{0.53}Mn_{0.47}O_4$ tetrahedron located at the center and tip of the cell, which is primarily due to the co-occupation of 2a position by Bi and Mn atoms, with Mn occupancy reaching 0.467. Owing to the unique characteristics of Mn, a portion of Bi^{3+} converts into Bi^{5+}, resulting in a partial positive charge that needs to be compensated by the defect oxygen, thereby leading to the formation of BiO[4].

For BMO structure, all Bi atoms are coordinated with eight oxygen atoms, while Mn atoms exhibit two valence states (+3 and +4). Mn (III) is coordinated with six oxygen atoms, whereas Mn (IV) is coordinated with five oxygen atoms[5].

For R-MnO_2 structure, the [1 × 2] tunnel frame of R-MnO_2 is composed of a double-stranded structure with shared angles, where the double-stranded structure is formed by a MnO_6 octahedron with shared edges, belonging to a sapphire structure[6].

For δ-BMO structure, the δ-BMO compound exhibits a two-dimensional layered structure with a layer spacing of approximately 0.7 nm. This structure is composed of MnO_6 octahedra, with the presence of Bi ions doped between the layers[6].

References

[1] Kresse, G. and Joubert, D., *Phy. Rev. B*, 1999, **59**, 1758-177.

[2] Perdew, J. P., Burke, K. and Ernzerhof, M., *Phy. Rev. Lett.*, 1996, **77**, 3865-3868.

[3] S. Grimme, J. Antony, S. Ehrlich and H. Krieg, *J. Chem. Phys.*, 2010, **132**. 154104.

[4] L. A. S. de Oliveira, J. P. Sinnecker, M. D. Vieira, and A. Pentón-Madrigal, *J. Appl. Phys.*, 2010, **107**, 09D907.

[5] J. Zhan and Y. Long, *Ceram. Int.*, 2018, **44**, 14891-14895.

[6] X. Chen, P. Ruan, X. Wu, S. Liang and J. Zhou, *Acta Phys. -Chim. Sin.*, 2022, **38**,

2111003-2111000.